
Interpretable Sequence Learning for COVID-19 Forecasting

Sercan Ö. Arik, Chun-Liang Li, Jinsung Yoon, Rajarishi Sinha, Arkady Epshteyn,
Long T. Le, Vikas Menon, Shashank Singh, Leyou Zhang, Martin Nikoltchev,
Yash Sonthalia, Hootan Nakhost, Elli Kanal, Tomas Pfister

Google Cloud AI

{soarik, chunliang, jinsungyoon, sinharaj, aepshtey, longtle, vikasmenon,
shashanksi, leyouz, mnikoltchev, yashks, hootan, ekanal, tpfister}@google.com

Abstract

We propose a novel approach that integrates machine learning into compartmental disease modeling (e.g., SEIR) to predict the progression of COVID-19. Our model is explainable by design as it explicitly shows how different compartments evolve and it uses interpretable encoders to incorporate covariates and improve performance. Explainability is valuable to ensure that the model’s forecasts are credible to epidemiologists and to instill confidence in end-users such as policy makers and healthcare institutions. Our model can be applied at different geographic resolutions, and we demonstrate it for states and counties in the United States. We show that our model provides more accurate forecasts compared to the alternatives, and that it provides qualitatively meaningful explanatory insights.

1 Introduction

The rapid spread of COVID-19, the disease caused by the SARS-CoV-2 virus, has had a significant impact on humanity. Accurately forecasting the progression of COVID-19 can help (i) healthcare institutions to ensure sufficient supply of equipment and personnel to minimize fatalities, (ii) policy makers to consider potential outcomes of their policy decisions, (iii) manufacturers and retailers to plan their business decisions based on predicted attenuation or recurrence of the pandemic and (iv) the general populace to have confidence in the choices made by the above actors.

Data is one of the greatest assets of the modern era, including for healthcare [1]. We aim to exploit this abundance of data for COVID-19 forecasting. From available healthcare supply to mobility indices, many information sources are expected to have predictive value for forecasting the spread of COVID-19. Data-driven time-series forecasting has enjoyed great success, particularly with advances in deep learning [2–4]. However, several features of the current pandemic limit the success of standard time-series forecasting methods:

- Because there is no close precedent for the COVID-19 pandemic, it is necessary to integrate existing data with priors based on epidemiological knowledge of disease dynamics.
- The data generating processes are non-stationary because progression of the disease influences public policy and individuals’ public behaviors, and vice versa.
- There are many potential sources of data, but their causal impact on the disease is unclear, and their impact on the progression of the disease is unknown.
- The problem is non-identifiable as most infected can be undocumented.
- Data sources are noisy due to reporting issues or due to data collection problems.
- Beyond accuracy, explainability is desired – the users, either from healthcare or policy or business angles, should be able to interpret the results in a meaningful way for optimal strategic planning.

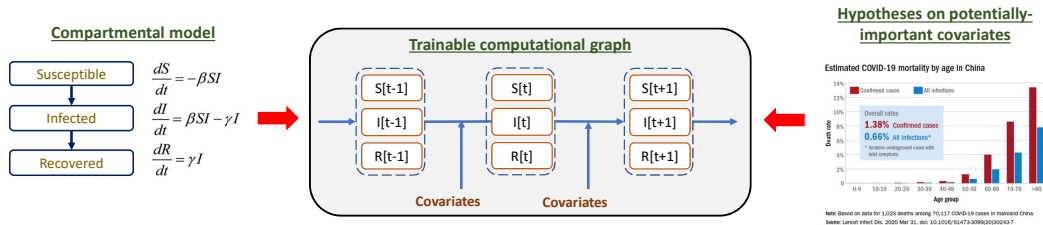


Figure 1: Our approach is based on distilling the inductive bias from compartmental models (as exemplified here for the popular SIR, Susceptible-Infected-Recovered, model) into a computational graph, where the transitions depend on the related covariates.

Compartmental models, such as the SIR and SEIR [5] models, are widely used for disease modeling by healthcare and public authorities. Such models represent the number of people in each of the compartments (see Fig. 1) and model the transitions between them via differential equations. Compartmental models often have several shortcomings: (i) only few learnable parameters resulting low model capacity (ii) non-stationary dynamics due to static rates in the differential equations; (iii) no covariates to extract information; (iv) assumptions on well-mixed compartments, i.e. each individual is statistically identical to others in the same compartment [6]; (v) no information sharing across time or geography, and (vi) non-identifiability – identical results may arise from different parametrizations [7].

While preserving interpretability for domain experts, we aim for accurate forecasts that go beyond the capabilities of standard compartmental models by utilizing rich datasets with high temporal and spatial granularity. Our approach is based on integrating covariate encoding into compartment transitions to extract relevant information via end-to-end learning (Fig. 1). In this way, we provide an inherently interpretable model that reflects the inductive biases of epidemiology. To get high accuracy, we introduce several innovative contributions:

1. We extend the standard SEIR model to also include compartments for undocumented cases and hospital resource usage. Our end-to-end modeling framework can infer meaningful estimates for undocumented cases even if there is no direct supervision for them.
2. The disease dynamics vary over time, e.g., as mobility reduces, the spreading would decay. To accurately reflect such dynamics, we propose time-varying encoding of the covariates.
3. We propose learning mechanisms to improve generalization while learning from limited training data, using (i) masked supervision from partial observations, (ii) partial teacher-forcing to minimize error propagation, (iii) regularization and (iv) cross-location information-sharing.

We demonstrate our approach for COVID-19 forecasting for the United States (US), the country that has suffered from the highest number of confirmed cases and deaths as of October 2020. For both at State- and County-level granularities, we show that our model outperforms commonly-used alternatives. Beyond accurate forecasts, we show how our model can be used for insights towards better understanding of COVID-19 pandemic.

2 Related work

Compartmental models: Using compartmental models [8] for infectious diseases can be dated back to [5], which has three compartments including susceptible, infected and recovered. Several infectious diseases, including COVID-19, manifest an incubation period during which an individual is infected, but are not yet spreaders. To this end, the Exposed (E) compartment is employed, yielding the SEIR model [9]. Beyond these basic types of compartment models, several other types of compartment models have been used, such as granular infections [10] and undocumented compartments [11]. A mixture of state-space model [12] in machine learning is presented in [13].

Integrating covariates into compartmental models: Policy changes such as travel bans or public restrictions have a marked, if local, effect on the disease progression. [14] designs a model that predict the effect of travel restrictions on the disease spread in China. [15] uses a modified SEIR model with mobility covariates to show the impact of interventions in the US. [16] presents a Bayesian hierarchical model for the effect of non-pharmaceutical interventions on COVID-19 in Europe. Such studies have typically been limited to the impact of one or two covariates, while our method models numerous static and time-varying ones in conjunction.

Disease modeling using machine learning: Apart from compartmental models, a wide variety of methods exist for modeling infectious disease. These include diffusion models [17], agent-based models [18], and cellular automata [19]. With the motivation of data-driven learning, some also integrate covariates into disease modeling, e.g. using LSTM-based models [20–22].

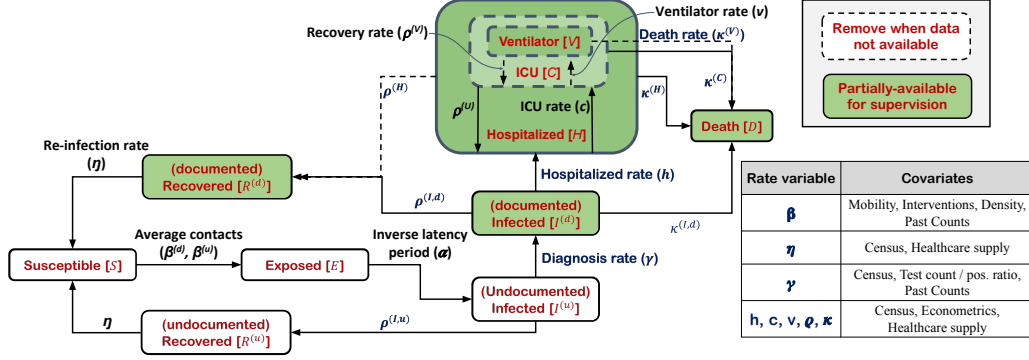


Figure 2: The modeled compartments and the corresponding covariates, with the legend on the right.

Learning from data and equations: Strong inductive biases can improve machine learning. One type of such bias is the set of equations between input and output, particularly common in physics or chemistry. To incorporate the inductive bias of equations, several recent works [23–26] have studied parametric approaches, as in our paper, where trainable models are incorporated to model only certain terms in the equations, while the equations still govern the end-to-end relationships.

Other COVID-19 forecasting works: Different works have adopted compartmental models for COVID-19 forecasting via modeling different compartments, such as YYG [27]. However, they do not leverage additional covariates. IHME [28] is based on fitting a curve to model the non-linear mixing effects, which does not explicitly model the transitions between the compartments. LANL [29] is based on statistical-dynamical growth modeling for the susceptible and infected cases.

3 Proposed compartmental model for COVID-19

We adapt the standard SEIR model with some major changes, as shown in Fig. 2:

- **Undocumented infected and recovered compartments:** Recent studies suggest that majority of the infected people are not detected and they dominate disease spreading¹ [30, 31] (as the documented ones are either self-isolated or hospitalized) An undocumented infected individual is able to spread the disease, until being documented or recovered without being undocumented.
- **Hospitalized, ICU and ventilator compartments:** We introduce compartments for the people who are hospitalized, in the ICU, or on a ventilator, as there is a demand to model these [32] and there is partially-available observed data to be used for supervision.
- **Partial immunity:** To date, there is no scientific consensus on what fraction of recovered cases demonstrate immunity to future infection. Due to reports of reinfection [33] we model the rate of reinfection from recovered compartments (though our model infers low reinfection rates).
- **Other Assumptions:** We assume the published COVID-19 death counts are coming from documented cases, not undocumented. Also, we assume that the entire population is invariant, i.e. births and non-Covid deaths are negligible in comparison to the entire population. Last, by data publishing frequency, we assume a fixed sampling interval of 1 day.

Table 1: Modeled compartments.

Compartment	Description	Compartment	Description
S	Susceptible	$R^{(u)}$	Recovered undocumented
E	Exposed	H	Hospitalized
$I^{(d)}$	Infected documented	C	In intensive care unit (ICU)
$I^{(u)}$	Infected undocumented	V	On ventilator
$R^{(d)}$	Recovered documented	D	Death

The modeled compartments are shown in Table 1. For a compartment X , $X_i[t]$ denotes the number of individuals in that compartment at location i and time t . $N[t]$ denotes the total population. Fig. 2 describes transition rate variables used to relate the compartments, via the equations (we omit the index i for concision):

¹[11] estimates that $> 80\%$ of cases in China were undocumented during the early phase of the pandemic.

$$\begin{aligned}
S[t] - S[t-1] &= -(\beta^{(d)}I^{(d)}[t-1] + \beta^{(u)}I^{(u)}[t-1])\frac{S[t-1]}{N[t-1]} + \eta(R^{(d)}[t-1] + R^{(u)}[t-1]), \\
E[t] - E[t-1] &= (\beta^{(d)}I^{(d)}[t-1] + \beta^{(u)}I^{(u)}[t-1])\frac{S[t-1]}{N[t-1]} - \alpha E[t-1], \\
I^{(u)}[t] - I^{(u)}[t-1] &= \alpha E[t-1] - (\rho^{(I,u)} + \gamma)I^{(u)}[t-1], \\
I^{(d)}[t] - I^{(d)}[t-1] &= \gamma I^{(u)}[t-1] - (\rho^{(I,d)} + \kappa^{(I,d)} + h)I^{(d)}[t-1], \\
R^{(u)}[t] - R^{(u)}[t-1] &= \rho^{(I,u)}I^{(u)}[t-1] - \eta R^{(u)}[t-1], \\
R^{(d)}[t] - R^{(d)}[t-1] &= \rho^{(I,d)}I^{(d)}[t-1] + \rho^{(H)}(H[t-1] - C[t-1]) - \eta R^{(d)}[t-1], \\
H[t] - H[t-1] &= hI^{(d)}[t-1] - (\kappa^{(H)} + \rho^{(H)})(H[t-1] - C[t-1]) - \kappa^{(C)}(C[t-1] - V[t-1]) - \kappa^{(V)}V[t-1], \\
C[t] - C[t-1] &= c(H[t-1] - C[t-1]) - (\kappa^{(C)} + \rho^{(C)} + v)(C[t-1] - V[t-1]) - \kappa^{(V)}V[t-1], \\
V[t] - V[t-1] &= v(C[t-1] - V[t-1]) - (\kappa^{(V)} + \rho^{(V)})V[t-1], \\
D[t] - D[t-1] &= \kappa^{(V)}V[t-1] + \kappa^{(C)}(C[t-1] - V[t-1]) + \kappa^{(H)}(H[t-1] - C[t-1]) + \kappa^{(I,d)}I^{(d)}[t-1],
\end{aligned}$$

Corollary: Basic reproduction number An analysis of our compartmental model using the Next-Generation Matrix method [34] yields the effective reproductive number (spectral radius) as:

$$R_e = \frac{\beta^{(d)}\gamma + \beta^{(u)}(\rho^{(I,d)} + \kappa^{(I,d)} + h)}{(\gamma + \rho^{(I,u)}) \cdot (\rho^{(I,d)} + \kappa^{(I,d)} + h)}. \quad (1)$$

Please see Appendix for derivations. Note that when $\gamma = 0$, our compartmental model reduces to the standard SEIR model with the undocumented infected and recovered. In this case, $R_0 = \beta^{(u)}/\rho^{(I,u)}$.

4 Encoding covariates

Time-varying modeling of variables: Instead of using static rate variables across time to model compartment transitions as in standard compartmental models, there should be time-varying functions that map them from known observations. For example, if human mobility decreases over time, the $S \rightarrow E$ transition should reflect that. Consequently, we propose replacing all static rate variables with learnable functions that output their value from the related static and time-varying covariates at each location and timestep. We list all the covariates used for each rate variable in the Appendix. We note that learnable encoding of variables still preserves the inductive bias of the compartmental modeling framework while increasing the model capacity via learnable encoders.

Interpretable encoder architecture: In addition to making accurate forecasts, it is valuable to understand how each covariate affects the model. Such explanations greatly help users from healthcare and public sector to understand the disease dynamics better, and also help model developers to ensure the model is learning appropriate dynamics via sanity checks with known scientific studies or common knowledge. To this end we adopt a generalized additive model [35] for each variable v_i from Table 2 based on additional *covariates* $\text{cov}(v_i, t)$ at different time t . The covariates we consider include (i) the set of static covariates \mathcal{S} , such as population density, and (ii) $\{f[t-j]\}_{f \in \mathcal{F}_i, j=1, \dots, k}$ the set of time-varying covariates (features) \mathcal{F}_i with the observation from $t-1$ to $t-k$, such as mobility. Omitting individual feature interactions and applying additive aggregation, we obtain

$$v_i[t] = v_{i,L} + (v_{i,U} - v_{i,L}) \cdot \sigma(c + b_i + \mathbf{w}^\top \text{cov}(v_i, t)), \quad (2)$$

where $v_{i,L}$ and $v_{i,U}$ are the lower and upper bounds of v_i for all t , c is the global bias, b_i is the location-dependent bias. \mathbf{w} is the trainable parameter, and $\sigma(\cdot)$ is the sigmoid function to limit the range to $[v_{i,L}, v_{i,U}]^2$, which is important to stabilize training and avoid overfitting. We note that although Eq. (2) denotes a linear decomposition for $v_i[t]$ at each timestep, the overall behavior is still highly non-linear due to the relationships between compartments.

Covariate forecasting: The challenge of using Eq. (2) for future forecasting is that some time-varying covariates are not available for the entire forecasting horizon. Assume we have the observations of covariates and compartments until T , and we want to forecast from $T+1$ to $T+\tau$. To forecast $v_i[T+\tau]$, we need the time varying covariates $f[T+\tau-k : T+\tau-1]$ for $f \in \mathcal{F}_i$, but some of them are not observed when $\tau > k$. To solve this issue, we propose to forecast $f[T+\tau-k : T+\tau-1]$ based on their own past observations until T , which is a standard one dimensional time series forecasting for a given covariate f at a given location. In this paper, we use a standard XGBoost model [36] which inputs time-series features.³

Information-sharing across locations: Some aspects of the disease dynamics are location-dependent while others are not. In addition, data availability varies across locations – there may be limited observations to learn the impact of a covariate. A model able to learn both location dependent

²We use $v_{i,L}=0$ for all variables, $v_{i,U} = 1$ for β , 0.2 for α , 0.001 for η and 0.1 for others.

³We used the lagged features of the past 7 days plus the 2 weeks ago, and mean/max in the windows of sizes of 3, 5, 7, 14 and 21 days.

and independent dynamics is desirable. Our encoders in Eq. (2) partially capture location-shared dynamics via shared \mathbf{w} and the global bias c . To allow the model capture remaining location-dependent dynamics, we introduce the local bias b_i . A challenge is that the model could ignore the covariates by encoding all information into b_i during training. This could hurt generalization as there would not be any information-sharing on how static covariates affect the outputs across locations. Thus, we introduce a regularization term $L_{ls} = \lambda_{ls} \sum_i |b_i|^2$ to encourage the model to leverage covariates and c for information-sharing instead of relying on b_i . Without L_{ls} , we observe that the model would use the local bias more than the encoded covariates, and suffers from poorer generalization.

5 End-to-end training

Algorithm 1 Pseudo-code for training the proposed model

Inputs: Forecasting horizon τ , compartment observations $Q_i, H_i, C_i, V_i, D_i, R_i$ from T_s until T , the number of fine tuning iterations F , loss coefficients λ_{R_e} and λ_{ls} .

Initialize trainable parameters $\theta = \{\mathbf{w}_i, c, b_i\}$, and initial conditions for the compartments $\hat{E}[0], \hat{I}^{(d)}[0], \hat{I}^{(u)}[0], \hat{R}^{(d)}[0], \hat{R}^{(u)}[0], \hat{H}[0], \hat{C}[0], \hat{V}[0], \hat{D}[0]$

Split τ day validation $Y_i[T - \tau : T]$ for all locations i , where $Y \in \{Q, H, C, V, D, R^{(d)}\}$

while until convergence **do**

Sample initial conditions $E_i[0], I_i^{(d)}[0], I_i^{(u)}[0], R_i^{(d)}[0], R_i^{(u)}[0], H_i[0], C_i[0], V_i[0], D_i[0]$

$\theta \leftarrow \theta - \text{RMSProp}(\nabla_{\theta} \mathcal{L}(T_s, T - \tau - 1))$

Update the optimal parameters: $\theta_{opt} = \theta$ if $L_{fit}[T - \tau : T]$ is the current-best

Final fine-tuning: fine-tune with joint training and validation data:

$\theta \leftarrow \theta_{opt}$

for F iterations **do**

$\theta \leftarrow \theta - \text{RMSProp}(\nabla_{\theta} \mathcal{L}(T_s, T))$

Update the optimal parameters: $\theta_{opt} = \theta$ if $L_{fit}[T - \tau : T]$ is the currently best

Output: Return θ_{opt}

Learning from partially-available observations: Fitting would have been easy with observations for all compartments, however, we only have access to some. For instance, $I^{(d)}$ is not given in the ground truth of US data but we instead have, Q , the total number of confirmed cases, that we use to supervise $I^{(d)} + R^{(d)} + H + D$. Note that $R^{(ud)}, I^{(ud)}, S, E$ are not given as well. Formally, we assume availability of the observations $Y[T_s : T]^4$, for $Y \in \{Q, H, C, V, D, R^{(d)}\}$, and consider forecasting the next τ days, $\hat{Y}[T + 1 : T + \tau]$.

Fitting objective: There is no direct supervision for training encoders, while they should be learned in an end-to-end way via the aforementioned partially-available observations. We propose the following objective for range $[T_s, T_e]$:

$$L_{fit}[T_s : T] = \sum_{Y \in \{Q, H, C, V, D, R^{(d)}\}} \lambda_Y \sum_{t=T_s}^{T-\tau} \sum_{i=1}^{\tau} \frac{\mathbb{I}(Y[t+i])}{\sum_j \mathbb{I}(Y[j]) \cdot Y[j]} \cdot q(t+i-T_s; z) \cdot L(Y[t+i], \hat{Y}[t+i]). \quad (3)$$

$\mathbb{I}(\cdot) \in \{0, 1\}$ indicates the availability of the Y to allow the training to focus only on available observations. $L(\cdot)$ is the loss between the ground truth and the predicted values (e.g., ℓ_2 or quantile loss), and λ_Y are the importance weights to balance compartments due to its robustness (e.g., D is much more robust than others). Lastly, $q(t; z) = \exp(t \cdot z)$ is a time-weighting function (when $z = 0$, there is no time weighting) to favor more recent observations with z as a hyperparameter.

Constraints and regularization: Given the limited dataset size, overfitting is a concern for high-capacity encoders trained on insufficient data. In addition to limiting the model capacity with the epidemiological inductive bias, we further apply regularization to improve generalization to unseen future data. An effective regularization is constraining the effective reproduction number R_e as derived in Eq. (1). There are rich literature in epidemiology on R_e to give us good priors on the range of the number should be. For a reproduction number $R_e[t]$ at time t , we consider the regularization

$$L_{R_e}[T_s : T] = \sum_{t=T_s}^T \exp((R_e[t] - R)_+),$$

⁴We use the notation $S_i[T_s : T]$ to denote all timesteps between T_s (inclusive) and T (inclusive).

where R is a prespecified *soft* upper bound. The regularization favors the model with R_e in a reasonable range in addition to good absolute forecasting numbers. In the experiment, we set $R = 5$ without further tuning. Last, ignoring the perturbation of a small local window, the trend of forecast should usually be smooth. One commonly used smoothness constraint, is on the first-order difference. We call it as *velocity*, which is defined as $v_Y[t] = (Y[t] - Y[t - k])/k$. The first-order constraint encourage $v_Y[t] \approx v_Y[t - 1]$, which causes linear forecasting, and cannot capture the rapid growing cases. Instead, we relax the smoothness to be on the second order difference. We called it as *acceleration*, which is defined as $a_Y[t] = v_Y[t] - v_Y[t - 1]$. The regularization is

$$L_{acc}[T_s:T] = \sum_{Y \in \{Q, D\}} \sum_{t=T_s+1}^T (a_Y[t] - a_Y[t - 1])^2$$

The final objective function is

$$\mathcal{L}(T_s, T) = L_{fit}[T_s : T] + \lambda_{ls} \cdot L_{ls} + \lambda_{R_e} \cdot L_{R_e}[T_s : T] + \lambda_{acc} \cdot L_{acc}[T_s : T], \quad (4)$$

where $L_{ls} = \lambda_{ls} \sum_i |b_i|^2$ as discussed in Sec. 4.

Partial teacher forcing: The compartmental model presented in Sec. 3 produces the future propagated values from the current timestep. During training, we have access to the observed values for $Y \in \{Q, H, C, V, D, R^{(d)}\}$ at every timestep, which we could condition the propagated values on, commonly-known as teacher forcing [37] to mitigate error propagation. At inference time, however, ground truth beyond the current timestep t is unavailable, hence the predictions should be conditioned on the future estimates. Using solely ground-truth to condition propagation would create a train-test mismatch. In the same vein of past research to mix the ground truth and predicted data to condition the projections on [38], we propose partial teacher forcing, simply conditioning $(1 - \nu \mathbb{I}\{Y[t]\})Y[t] + \nu \mathbb{I}\{Y[t]\} \hat{Y}[t]$, where $\mathbb{I}\{Y[t]\} \in \{0, 1\}$ indicates whether the ground truth $Y[t]$ exists and $\nu \in [0, 1]$. In the first stage of training, we use teacher forcing with $\nu \in [0, 1]$, which is a hyperparameter. For fine-tuning (please see below), we use $\nu = 1$ to unroll the last τ steps to mimic the real forecasting scenario.

Model fitting and selection: The training pseudo code is presented in Algorithm 1. We split the observed data into training and validation with the last τ timesteps to mimic the testing scenario. We use the training data for optimization of the trainable degrees of freedom, collectively represented as θ , while the validation data is used for early stopping and model selection. Once the model is selected, we fix the hyperparameters and run fine-tuning on joint training and validation data, to not waste valuable recent information by using it only for model selection. For optimization, we use RMSProp as it is empirically observed to yield lower losses compared to other algorithms and providing the best generalization performance.

6 Experiments

Ground truth data: We conduct all experiments on US COVID-19 data. The primary ground truth data for the progression of the disease, for Q and D , are from [39] as used by several others, e.g. [28]. They obtain the raw data from the state and county health departments. Because of the rapid progression of the pandemic, past data has often been restated, or the data collection protocols have been changed. Ground truth data for the H , C and V (see Fig. 1) are obtained from [40]. Note that there are significant restatements of the past observed counts in the data, so we use the reported numbers on the prediction date for training (although later we know the restated past ground truth), and the reported numbers τ days after prediction date for evaluation, to be completely consistent with other models for fair comparison.

Covariates: The progression of COVID-19 is influenced by a multitude of factors, including relevant properties of the population, health, environmental, hospital resources, demographics and econometrics indicators. Time-varying factors such as population mobility, hospital resource usage and public policy decisions can also be important. However, indiscriminately incorporating a data source may have deleterious effects. Thus, we curate our data sources to limit them to one source in each category of factors that may have predictive power at the corresponding transition. We use datasets from public sources (please see Appendix for details). We apply forward- and backward-filling imputation (respectively) for time-varying covariates, and median imputation for static covariates. Then, all covariates are normalized to be in $[0, 1]$, considering statistics across all locations and time-steps.

Training: We implement Algorithm 1 in TensorFlow at state- and county-levels, using ℓ_2 loss for point forecasts. We employ [41] for hyperparameter tuning (including all the loss coefficients,

learning rate, and initial conditions) with the objective of optimizing for the best validation loss, with 400 trials and we use $F = 300$ fine-tuning iterations. We choose the compartment weights $\lambda^D = \lambda^Q = 0.1$, $\lambda^H = 0.01$ and $\lambda^{R^{(d)}} = \lambda^C = \lambda^V = 0.001$.⁵ At county granularity, we do not have published data for C and V , so, we remove them along with their connected variables.

6.1 Results

Table 2: τ -day average MAE for forecasting the number of deaths at state-level. Since benchmark models from covid19-forecast-hub repository release forecasts at different dates and horizons, not all models have predictions for all prediction dates/horizons (indicated by “—”). **Bold** indicates the best.

Pred. horizon τ (days)	Pred. date	Ours	CU	LANL	UT	YYG
14	05/19/2020	35.8	71.4	45.3	43.7	46.5
	05/26/2020	29.4	58.5	36.3	43.8	37.7
	06/02/2020	32.8	86.1	33.5	35.1	26.5
	06/09/2020	28.8	71.0	34.7	33.5	22.3
	06/16/2020	31.4	79.6	50.8	48.9	32.1
	06/23/2020	63.8	134.7	85.8	67.7	64.2
	06/30/2020	46.5	152.1	48.6	34.1	35.1

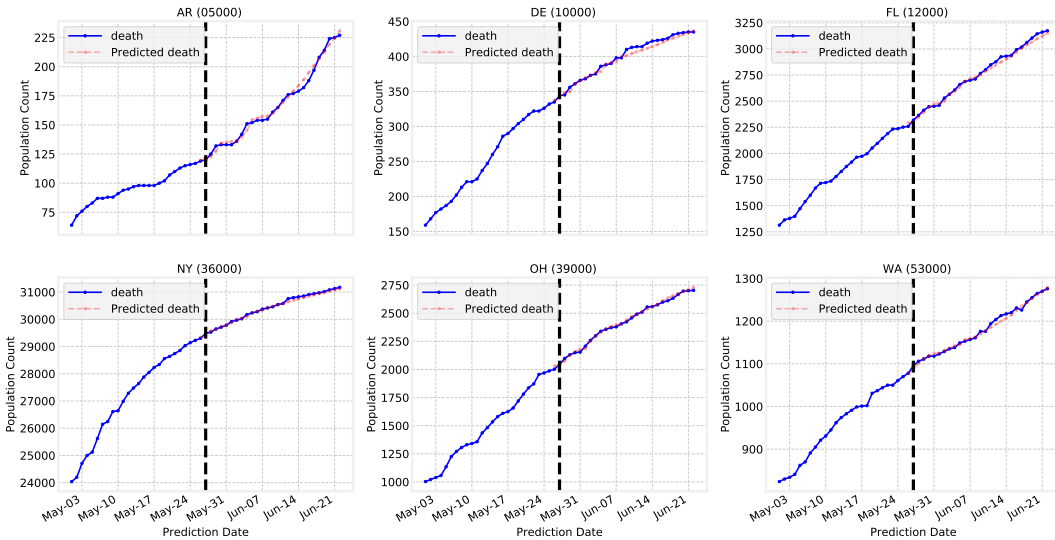


Figure 3: Ground-truth vs. predicted 14-day death forecasts for 6 states: AR, DE, FL, NY, OH, and WA on 06/09/2020.

State-level forecasts: Fig. 3 exemplifies the forecasting performance of our model on 4 states. We compare our method to widely-used benchmarks for state-level prediction of the number of deaths in each US state. Specifically, we report comparisons with Columbia University (CU) model [42], the GrowthRate model from Los Alamos National Laboratory (LANL) [29], UT-Austin (UT) model [43] and the YYG model [27]. CU is a metapopulation SEIR model with a selection mechanism among the different generated scenarios for interventions. LANL is based on statistical-dynamical growth modeling for the underlying numbers of susceptible and infected cases. UT makes predictions assuming that social distancing patterns, as measured by anonymized mobile-phone GPS traces, using a Bayesian multilevel negative binomial regression model. YYG is an SEIR model with learnable parameters and accounts for reopenings. The parameters are fit using hyperparameter optimization. Unlike ours, YYG uses fixed (time-invariant) rates as SEIR parameters and is limited to modeling standard SEIR compartments. Note that, in contrast to usual benchmarks, these models may change significantly between forecast dates. Table 2 shows comparisons for different prediction dates and forecasting horizons τ . Our model is consistently accurate across phases of the pandemic and outperforms all others except YYG by a large margin. YYG is merely optimized for the number of deaths, whereas our model jointly predicts all the compartments while being explainable. Fig. 3 exemplifies our forecasting on different states, and shows our model can forecast well on different scale of reported deaths.

⁵Our results are not highly sensitive to these.

Table 3: τ -day average MAE for 14-day forecasting of the number of deaths for county-level forecasts.

Pred. horizon τ (days)	Pred. date	Ours	Berkeley CLEP
14	05/19/2020	1.19	1.91
	06/09/2020	1.02	1.79
	05/19/2020	1.80	3.24
	05/26/2020	1.56	3.10
	06/09/2020	1.36	3.20
	06/16/2020	1.37	3.32

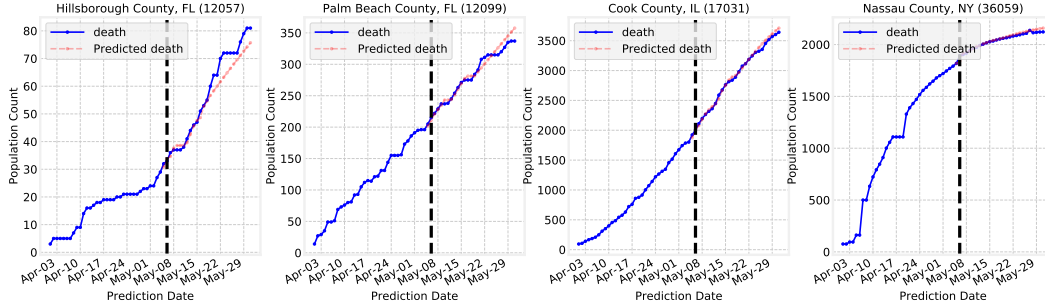


Figure 4: Ground-truth vs. predicted 14-day death forecasts for 4 counties: Hillsborough Co., FL; Palm Beach Co., FL; Cook Co., IL; Nassau Co., NY on 05/19/2020.

County-level forecasts: Table 3 shows the performance of our model on all (more than 3000) US counties. Compared with state-level forecasting, it is more challenging due to sparse observations. We compare our method to predictions by Berkeley Yu model [44] for the number of deaths in each US county. The model comprises several predictors (including exponential and linear) and ensemble their forecasts resulting Combined Linear and Exponential Predictors (CLEP). The setting to compare the county is same as state-level comparisons. Table 3 demonstrates that our model yields much lower error compared to the Berkeley CLEP model. Fig. 4 exemplifies the prediction for a few counties.

6.2 Ablation studies

Table 4: τ -day average MAE for 14-day forecasting of the number of deaths at state-level.

Models / Prediction date	05/25/2020	06/01/2020	06/08/2020
Standard SEIR compartments (w/o encoder)	87.3	76.1	71.0
Standard SEIR compartments (with encoder)	50.0	37.5	39.3
Our model (w/o encoder)	69.2	36.8	28.7
Our model w/o fine-tuning	94.1	78.7	65.8
Our model w/o partial teacher forcing	792.6	1903.8	1289.7
Our model	32.9	23.8	26.5

Table 4 presents the major results for ablation cases. For these ablation studies, to merely focus on the impact of the model changes, we use the most recently-updated data for both training and evaluation. We observe the significant benefits of (i) learning rates from covariates with encoders, (ii) modeling extra compartments and supervision from H , C and V , (iii) partial teacher forcing and (iv) final-fine tuning, adapting to the most recent data after model selection based on validation.

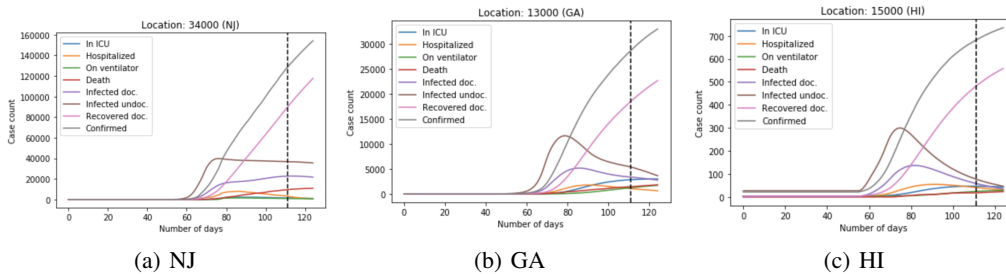


Figure 5: Fitted compartments for (a) NJ, (b) GA and (c) HI, where vertical lines show the forecasting starting timestep. Note that infected values are not cumulative, thus decay over time while the confirmed keeps increasing. These can be used to gain insights in disease evolution, e.g. we observe the increasing trend of the number of confirmed cases more sharply in NJ, whereas it is saturating in HI, due to the sharp decrease in the number of infected people after the peak.

6.3 Extracting explainable insights

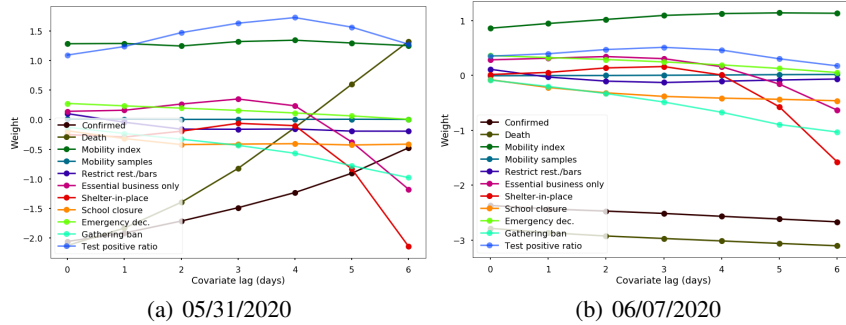


Figure 6: Learned weights of covariates for $\beta^{(u)}$, for 7-day state-level forecasting models on 05/31/2020 and 06/07/2020. Mobility index consistently has highly-positive impact on $\beta^{(u)}$, while gathering bans, school closures and shelter-in-place interventions have highly-negative impact. The magnitude of the weights for interventions get larger after a lag of few days.

The interpretability of our model is two fold. First, we model the compartments explicitly, thus our model provides insights into how the disease evolves. Fig 5 shows the fitted curves that can be used to infer important insights on where the peaking occurs, or the current decay trends. We observe the ratio of undocumented to documented infected at different phases, as well as the amount of increase/decrease for each compartment. Second, our model uses interpretable encoders, as discussed in Sec. 4. Ignoring co-linearity between covariates, rough insights can be inferred. Fig. 6 shows the learned weights of the time-varying covariates for $\beta^{(u)}$. The weights of the past days seem similar – the model averages them with slight decay in trends. For intervention covariates, the largest weights occur after a lag of a few days, suggesting their effectiveness after some lag. The positive weights of the mobility index, and negative weights of public interventions are clearly observed. Similar analysis can be performed on other variables as well. For γ , we observe the positive correlation of the positive ratio of tests. For static covariates, the insights are less apparent, but we observe meaningful learned patterns like the positive correlation of the number of households on public assistance or food stamps, population density and 60+ year old population ratio, on death rates.

6.4 Forecasting prediction intervals

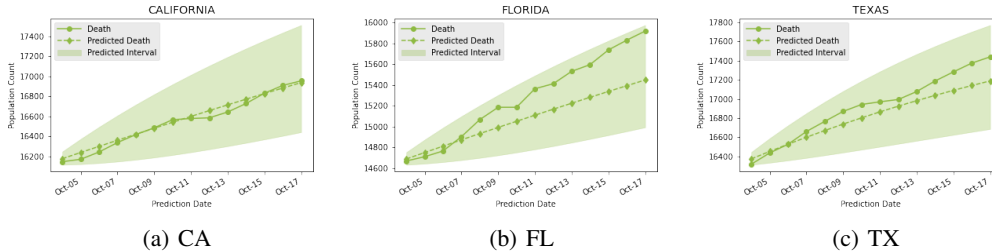


Figure 7: Prediction intervals for 14-day forecasting. We use the 10-th and the 90-th quantile prediction as the the lower and the upper bound of prediction intervals, respectively.

Besides point forecasts, prediction intervals could be helpful for healthcare and public policy planners, to consider a range of possible scenarios. Our framework allows the capability of modeling prediction interval forecasts, for which we replacing the L2 loss with weighted interval loss [45] in Eq. (3) and mapping the scalar propagated values to the vector of quantile estimates. For this mapping, we use the features $Y[t]/\hat{Y}[t]$ and $\mathbb{I}\{Y[t]\}$ for $T - \tau \leq t \leq T - 1$. We obtain the quantiles applying a linear kernel on these features, followed by ReLU and cumulative summation (to guarantee monotonicity of quantiles) and lastly normalization (to match the median to the input scalar point forecast from the proposed model). Fig. 7 exemplifies well-calibrated prediction interval forecasts – the ranges tend to be wider when there are non-smooth behaviors in data.

7 Conclusions

We propose an approach to modelling infectious disease progression by incorporating covariates into a domain-specific encoding, understandable by experts. We compare predictions for this novel model with state-of-the-art models and show that disaggregating the infected compartment into sub-compartments relevant to decision-making can make the model more useful to decision-makers.

8 Acknowledgements

Contributions of Nathanael C. Yoder, Michael W. Dusenberry, Dario Sava, Jasmin Repenning, Andrew Moore, Matthew Siegler, Ola Rozenfeld, Isaac Jones, Rand Xie, Brian Kang, Vishal Karande, Shane Glass, Afraz Mohammad, David Parish, Ron Bodkin, Hanchao Liu, Yong Li, Karthik Ramasamy, Priya Rangaswamy, Andrew Max, Tin-yun Ho, Sandhya Patil, Rif A. Saurous, Matt Hoffman, Peter Battaglia, Oriol Vinyals, Jeremy Kubica, Jacqueline Shreibati, Michael Howell, Meg Mitchell, George Teoderici, Kevin Murphy, Helen Wang, Tulsee Doshi, Garth Graham, Karen DeSalvo, and David Feinberg are gratefully acknowledged.

Broader Impact

COVID-19 is an epidemic that is affecting almost all countries in the world at the moment. As of the first week of June, more than 6.5 million people have been infected, resulting in more than 380k fatalities unfortunately. The economical and sociological impacts of COVID-19 are significant, and will be felt for many years to come.

Forecasting of the severity of COVID-19 is crucial, for healthcare providers to deliver the healthcare support for those who will be in the most need, for governments to take the most optimal policy actions while minimizing the negative impact of the outbreak, and for business owners to make crucial decisions on when and how to restart their businesses. With the motivation of helping all these actors, we propose a machine learning-based forecasting model that significantly outperforms any alternative methods, including the ones used by the healthcare providers and public sector. Not only are our forecasts far more accurate, our model is explainable by design. It is aligned with how epidemiology experts approach the problem, and the machine learnable components shed light on what data features have the most impact on the outcomes. These would be crucial for data-driven understanding of COVID-19, that can help domain experts for effective medical and public health decision-making.

Besides COVID-19 forecasting, our approach is in the direction of ingesting data-driven learning while using the inductive bias of differential equations, while representing the input-output relationships at a system-level. Not only infectious disease modeling, but numerous scientific fields that use such equations, such as Physics, Environmental Sciences, Chemistry etc. are expected to benefit from our contributions.

References

- [1] Stanford Health. Harnessing the power of data in health, June 2017.
- [2] Bryan Lim, Sercan O. Arik, Nicolas Loeff, and Tomas Pfister. Temporal fusion transformers for interpretable multi-horizon time series forecasting. *arXiv:1912.09363*, 2019.
- [3] David Salinas, Valentin Flunkert, and Jan Gasthaus. Deepar: Probabilistic forecasting with autoregressive recurrent networks. *arXiv:1704.04110*, 2017.
- [4] Boris N. Oreshkin, Dmitri Carpov, Nicolas Chapados, and Yoshua Bengio. N-beats: Neural basis expansion analysis for interpretable time series forecasting. *arXiv:1905.10437*, 2019.
- [5] W. O. Kermack and A. G. McKendrick. Contributions to the mathematical theory of epidemics—i, 1927.
- [6] Ping Yan and Gerardo Chowell. *Beyond the Initial Phase: Compartment Models for Disease Transmission*, chapter 4, pages 1–27. Springer International Publishing, 2019.
- [7] Kimberlyn Roosa and Gerardo Chowell. Assessing parameter identifiability in compartmental dynamic models using a computational approach: application to infectious disease transmission models. *Theoretical Biology and Medical Modelling*, 16, 12 2019.
- [8] David Smith and Lang Moore. The sir model for spread of disease, 2004.
- [9] Julie C. Blackwood and Lauren M. Childs. An introduction to compartmental modeling for the budding infectious disease modeler. *Letters in Biomathematics*, 5(1):195–221, 2018.

- [10] Grand Rounds. Covid-19 forecasting: Fit to a curve or model the disease in real-time?, 2020. <https://grandrounds.com/blog/covid-19-forecasting-fit-to-a-curve-or-model-the-disease-in-real-time/>, Last accessed on 2020-05-29.
- [11] Ruiyun Li, Sen Pei, Bin Chen, Yimeng Song, Tao Zhang, Wan Yang, and Jeffrey Shaman. Substantial undocumented infection facilitates the rapid dissemination of novel coronavirus (sars-cov-2). *Science*, 368(6490):489–493, 2020.
- [12] Daphne Koller and Nir Friedman. *Probabilistic graphical models: principles and techniques*. MIT press, 2009.
- [13] Dave Osthus, Kyle S Hickmann, Petruța C Caragea, Dave Higdon, and Sara Y Del Valle. Forecasting seasonal influenza with a state-space SIR model. *The annals of applied statistics*, 11(1):202, 2017.
- [14] Matteo Chinazzi, Jessica T. Davis, Marco Ajelli, Corrado Gioannini, Maria Litvinova, Stefano Merler, Ana Pastore y Piontti, Kunpeng Mu, Luca Rossi, Kaiyuan Sun, Cécile Viboud, Xinyue Xiong, Hongjie Yu, M. Elizabeth Halloran, Ira M. Longini, and Alessandro Vespignani. The effect of travel restrictions on the spread of the 2019 novel coronavirus (covid-19) outbreak. *Science*, 368(6489):395–400, 2020.
- [15] Sen Pei, Sasikiran Kandula, and Jeffrey Shaman. Differential effects of intervention timing on covid-19 spread in the united states. *medRxiv*, 2020.
- [16] Seth Flaxman, Swapnil Mishra, Axel Gandy, H. Unwin, Helen Coupland, Thomas Mellan, Harrison Zhu, Tresnia Berah, Jeffrey Eaton, Pablo Guzman, Nora Schmit, Lucia Callizo, Imperial Team, Charles Whittaker, Peter Winskill, Xiaoyue Xi, Azra Ghani, Christl Donnelly, Steven Riley, and Samir Bhatt. Report 13 - estimating the number of infections and the impact of non-pharmaceutical interventions on covid-19 in 11 european countries, 04 2020.
- [17] Vincenzo Capasso. Reaction-diffusion models for the spread of a class of infectious diseases. In H. Neunzert, editor, *Proceedings of the Second European Symposium on Mathematics in Industry*, volume 3, pages 181–194. Springer, Dordrecht, 1988.
- [18] Elizabeth Hunter, Brian Mac Namee, and John Kelleher. An open-data-driven agent-based model to simulate infectious disease outbreaks. *PLoS ONE*, 13(12), 2018.
- [19] S. Hoya White, A. Martín del Rey, and G. Rodríguez Sánchez. Modeling epidemics using cellular automata. *Applied Mathematics and Computation*, 186(1):193–202, 2006.
- [20] S. R. Venna, A. Tavanaei, R. N. Gottumukkala, V. V. Raghavan, A. S. Maida, and S. Nichols. A novel data-driven model for real-time influenza forecasting. *IEEE Access*, 7:7691–7701, 2019.
- [21] Zifeng Yang, Zhiqi Zeng, Ke Wang, Sook-San Wong, Wenhua Liang, Mark Zanin, Peng Liu, Xudong Cao, Zhongqiang Gao, Zhitong Mai, Jingyi Liang, Xiaoqing Liu, Shiyue Li, Yimin Li, Feng Ye, Weijie Guan, Yifan Yang, Fei Li, Shengmei Luo, and Jianxing He. Modified seir and ai prediction of the epidemics trend of covid-19 in china under public health interventions. *Journal of Thoracic Disease*, 12:165–174, 03 2020.
- [22] Lijing Wang, Jiangzhuo Chen, and Madhav Marathe. Tdefsi: Theory guided deep learning based epidemic forecasting with synthetic information, 2020.
- [23] Sam Greydanus, Misko Dzamba, and Jason Yosinski. Hamiltonian neural networks. *arXiv:1906.01563*, 2019.
- [24] Miles Cranmer, Sam Greydanus, Stephan Hoyer, Peter Battaglia, David Spergel, and Shirley Ho. Lagrangian neural networks, 2020.
- [25] Michael Lutter, Christian Ritter, and Jan Peters. Deep lagrangian networks: Using physics as model prior for deep learning. *arXiv:1907.04490*, 2019.
- [26] Iclr 2020 workshop on integration of deep neural models and differential equations. <http://iclr2020deepdiffeq.rice.edu/>. Accessed: 2020-06-04.

- [27] YYG model for COVID-19 forecasting. <https://covid19-projections.com>. Accessed: 2020-06-04.
- [28] Christopher JL Murray. Forecasting covid-19 impact on hospital bed-days, icu-days, ventilator-days and deaths by us state in the next 4 months. *medRxiv*, 2020.
- [29] GrowthRate model from Los Alamos National Laboratory. <https://covid-19.bsvgateway.org/#link%20to%20forecasting%20site>. Accessed: 2020-06-04.
- [30] Xinmiao Fu. Global analysis of daily new covid-19 cases reveals many static-phase countries including us and uk potentially with unstoppable epidemics. *medRxiv*, 2020.
- [31] Yong-Shang Long, Zheng-Meng Zhai, Li-Lei Han, Jie Kang, Yi-Lin Li, Zhao-Hua Lin, Lang Zeng, Da-Yu Wu, Chang-Qing Hao, Ming Tang, Zonghua Liu, and Ying-Cheng Lai. Quantitative assessment of the role of undocumented infection in the 2019 novel coronavirus (covid-19) pandemic. *arXiv:2003.12028*, 03 2020.
- [32] E. Lee Daugherty Biddison, Howard S. Gwon, Monica Schoch-Spana, Alan C. Regenberg, Chrissie Juliano, Ruth R. Faden, and Eric S. Toner. Scarce resource allocation during disasters: A mixed-method community engagement study. *Chest*, 153(1):187–195, Jan 2018.
- [33] Robert D. Kirkcaldy, Brian A. King, and John T. Brooks. Covid-19 and postinfection immunity: Limited evidence, many remaining questions. *JAMA*, May 2020.
- [34] P. van den Driessche and J. Watmough. *Further Notes on the Basic Reproduction Number*, chapter 6, pages 159–178. Lecture Notes in Mathematics, LNM vol 1945. Springer, Berlin, Heidelberg, 2008.
- [35] Trevor Hastie and Robert Tibshirani. Generalized additive models. *Statist. Sci.*, 1(3):297–310, 08 1986.
- [36] Tianqi Chen and Carlos Guestrin. Xgboost: A scalable tree boosting system. In *Proceedings of the 22nd ACM SIGKDD International Conference on Knowledge Discovery and Data Mining*, page 785–794, New York, NY, USA, 2016. Association for Computing Machinery.
- [37] R. J. Williams and D. Zipser. A learning algorithm for continually running fully recurrent neural networks. *Neural Computation*, 1(2):270–280, 1989.
- [38] Samy Bengio, Oriol Vinyals, Navdeep Jaitly, and Noam Shazeer. Scheduled sampling for sequence prediction with recurrent neural networks. *arXiv:1506.03099*, 2015.
- [39] Hongru Ensheng Dong, Du and Lauren Gardner. An interactive web-based dashboard to track covid-19 in real time. *The Lancet Infectious Diseases*, 20(5):533–534, 2020.
- [40] Covid-Tracking. The covid tracking project, 2020.
- [41] Daniel Golovin, Benjamin Solnik, Subhodeep Moitra, Greg Kochanski, John Karro, and D. Sculley. Google vizier: A service for black-box optimization. In *Proceedings of the 23rd ACM SIGKDD International Conference on Knowledge Discovery and Data Mining*, pages 1487–1495. ACM, 2017.
- [42] Shaman group. <https://blogs.cuit.columbia.edu/jls106/publications/covid-19-findings-simulations/>. Accessed: 2020-06-04.
- [43] The university of texas covid-19 modeling consortium. <https://covid-19.tacc.utexas.edu/projections/>. Accessed: 2020-06-04.
- [44] Nick Altieri, Rebecca Barter, James Duncan, Raaz Dwivedi, Karl Kumbier, Xiao Li, Robert Netzorg, Briton Park, Chandan Singh, Yan Shuo Tan, et al. Curating a covid-19 data repository and forecasting county-level death counts in the united states. *arXiv:2005.07882*, 2020.
- [45] Johannes Bracher, Evan L. Ray, Tilmann Gneiting, and Nicholas G. Reich. Evaluating epidemic forecasts in an interval format, 2020.

- [46] Patrick Bryant and Arne Elofsson. Estimating the impact of mobility patterns on covid-19 infection rates in 11 european countries. *medRxiv*, 2020.
- [47] Michael S. Warren and Samuel W. Skillman. Mobility changes in response to covid-19. *arXiv:2003.14228 [cs.SI]*, 3 2020.
- [48] Realtime tracking of state-wide npi implementations. <https://c19hcc.org/resources/npi-dashboard/>. Accessed: 2020-06-04.
- [49] Xiao Wu, Rachel C. Nethery, Benjamin M. Sabath, Danielle Braun, and Francesca Dominici. Exposure to air pollution and covid-19 mortality in the united states: A nationwide cross-sectional study. *medRxiv*, 2020.
- [50] Bigquery public datasets. <https://cloud.google.com/bigquery/public-data>. Accessed: 2020-06-04.
- [51] Steven Sanche, Yen Ting Lin, Chonggang Xu, Ethan Romero-Severson, Nick Hengartner, and Ruian Ke. High contagiousness and rapid spread of severe acute respiratory syndrome coronavirus 2. *Emerging Infectious Diseases*, 26(7), July 2020.
- [52] Neil Pearce, Jan P. Vandenbroucke, Tyler J. VanderWeele, and Sander Greenland. Accurate statistics on covid-19 are essential for policy guidance and decisions. *American Journal of Public Health*, 110(7):949–951, 2020.
- [53] Norman Fenton, Graham A. Hitman, Martin Neil, Magda Osman, and Scott McLachlan. Causal explanations, error rates, and human judgment biases missing from the covid-19 narrative and statistics. *PsyArXiv:10.31234/osf.io/p39a4*, 2020.
- [54] Charles Blundell, Julien Cornebise, Koray Kavukcuoglu, and Daan Wierstra. Weight uncertainty in neural networks. *arXiv:1505.05424*, 2015.
- [55] Wesley Maddox, Timur Garipov, Pavel Izmailov, Dmitry P. Vetrov, and Andrew Gordon Wilson. A simple baseline for bayesian uncertainty in deep learning. *arXiv:1902.02476*, 2019.

A Datasets

As discussed, vast numbers of candidate datasets exist that could be related to the problem of COVID-19 forecasting. However, these datasets cannot be used indiscriminately. We select data sources based on whether they could have a predictive signal for the disease outcomes. Selecting multiple datasets from the same class of causes can obfuscate their predictive power. Therefore, we select datasets, one each from the classes of econometrics, demographics, mobility, non-pharmaceutical interventions, hospital resource availability, historical air quality. From each of these datasets, we further select covariates that could have an impact on the model compartments. We allow covariates to influence only those compartments (and hence transition rates) on which we posit that there exists a causal relationship (Table 5).

Ground Truth. We obtain primary ground truth for this work from the Johns Hopkins COVID-19 dataset [39]. Additional ground truth data that is used in the models for US states are obtained from the Covid Tracking Project [40].

Mobility. We posit that human mobility with a region, for work and personal reasons, has an effect on the average contact rates [46]. We use temporal mobility indices provided by Descartes labs at both state- and county-level resolutions [47]. These temporal indices are encoded to affect the average contact rates ($\beta^{(d)}$, $\beta^{(u)}$), at both the state- and county-level of geographic resolution.

Non-Pharmaceutical Interventions. We posit that public policy decisions restricting certain classes of population movement or interaction can have a beneficial effect on restricting the progression of the disease [15], at the state-level of geographic resolution. The interventions are presented in 6 binary valued time series indicating when an intervention has been activated in one of six categories—school closures, restrictions on bars and restaurants, movement restrictions, mass gathering restrictions, essential businesses declaration, and emergency declaration [48]. This temporal covariate is encoded into the average contact rates ($\beta^{(d)}$, $\beta^{(u)}$).

Table 5: Covariates selected for model.

Covariate	Variables that the covariate affect
Per capita income	$\beta^{(d)}, \beta^{(u)}, \eta, \gamma, \rho^{(I,d)}, \rho^{(I,u)}, \rho^{(H)}, \rho^{(C)}, \rho^{(V)}, h, c, v, \kappa^{(I,d)}, \kappa^H, \kappa^C, \kappa^V$
Population density	$\beta^{(d)}, \beta^{(u)}, \eta, \gamma, \rho^{(I,d)}$
Households on food stamps	$\eta, \rho^{(I,d)}, \rho^{(I,u)}, \rho^{(H)}, \rho^{(C)}, \rho^{(V)}, h, c, v, \kappa^{(I,d)}, \kappa^H, \kappa^C, \kappa^V$
Population	All
Number of households	$\beta^{(d)}, \beta^{(u)}, \eta, \gamma, \rho^{(I,d)}, \rho^{(I,u)}, \rho^{(H)}, \rho^{(C)}, \rho^{(V)}, h, c, v, \kappa^{(I,d)}, \kappa^H, \kappa^C, \kappa^V$
Population ratio above age 60	$\beta^{(d)}, \beta^{(u)}, \eta, \gamma, \rho^{(I,d)}, \rho^{(I,u)}, \rho^{(H)}, \rho^{(C)}, \rho^{(V)}, h, c, v, \kappa^{(I,d)}, \kappa^H, \kappa^C, \kappa^V$
Hospital rating scale	$\eta, \gamma, \rho^{(I,d)}, \rho^{(I,u)}, \rho^{(H)}, \rho^{(C)}, \rho^{(V)}, h, c, v, \kappa^{(I,d)}, \kappa^H, \kappa^C, \kappa^V$
Available types of hospitals	$\eta, \rho^{(I,d)}, \rho^{(I,u)}, \rho^{(H)}, \rho^{(C)}, \rho^{(V)}, h, c, v, \kappa^{(I,d)}, \kappa^H, \kappa^C, \kappa^V$
Hospital patient experience rating	$\eta, \rho^{(I,d)}, \rho^{(I,u)}, \rho^{(H)}, \rho^{(C)}, \rho^{(V)}, h, c, v, \kappa^{(I,d)}, \kappa^H, \kappa^C, \kappa^V$
Air quality measures	$\beta^{(d)}, \beta^{(u)}, \eta, \kappa^{(I,d)}$; also for state model: $h, c, v, \kappa^H, \kappa^C, \kappa^V$ and for county model: $\gamma, \rho^{(I,d)}, \rho^{(I,u)}$
Mobility indices	$\beta^{(d)}, \beta^{(u)}$
Non-pharmaceutical interventions (state model)	$\beta^{(d)}, \beta^{(u)}$
Total tests (state model)	γ, h
Confirmed per Total tests	$\beta^{(d)}, \beta^{(u)}, \gamma, h$
Confirmed Cases (lagged)	$\beta^{(d)}, \beta^{(u)}, \gamma, h$
Deaths (lagged)	$\beta^{(d)}, \beta^{(u)}, \gamma, h$

Demographics. We posit that the age of the individual has a significant outcome on the severity of the disease and the mortality. The Kaiser Family Foundation (On BigQuery at `c19hcc-info-ext-data:c19hcc_info_public.Kaiser_Health_demographics_by_Counties.States`) reports the number of individuals over the age of 60 in different US counties. We encode the effect of this static covariate into the average contact rate ($\beta^{(d)}, \beta^{(u)}$), the diagnosis (γ), re-infected (η), recovery ($\rho^{(I,d)}, \rho^{(I,u)}, \rho^{(H)}, \rho^{(C)}, \rho^{(V)}$) and death rates ($\kappa^{(I,d)}, \kappa^H, \kappa^C, \kappa^V$), at both the state- and county-level of geographic resolution.

Historical Air Quality. We posit that the historical ambient air quality in a region can have a deleterious effect on COVID-19 morbidity and mortality [49]. We use the BigQuery public dataset that comes from the US Environmental Protection Agency (EPA) that documents historical air quality indices at the county level (`bigquery-public-data:epa_historical_air_quality.pm10_daily_summary`). This static covariate is encoded into the recovery rates (η), recovery ($\rho^{(I,d)}, \rho^{(I,u)}, \rho^{(H)}, \rho^{(C)}, \rho^{(V)}$) and death rates ($\kappa^{(I,d)}, \kappa^H, \kappa^C, \kappa^V$), at both the state- and county-level of geographic resolution.

Econometrics. We posit that an individual’s economic status, as well as the proximity to other individuals in a region has an effect on the rates of infection, hospitalization and recovery. The proximity can be due to high population density in urban areas, or due to economic compulsions. The US census—available from `census.gov` and on BigQuery Public Datasets [50]—reports state- and county-level static data on population, population density, per capita income, poverty levels, households on public assistance (`bigquery-public-data:census_bureau_acs.county_2018_5yr` and `bigquery-public-data:census_bureau_acs.county_2018_1yr`). All of these measures affect transitions into the exposed and infected compartments ($\beta^{(d)}, \beta^{(u)}$), as well as the recovery rates ($\rho^{(I,d)}, \rho^{(I,u)}, \rho^{(H)}, \rho^{(C)}, \rho^{(V)}$) and death rates ($\kappa^{(I,d)}, \kappa^H, \kappa^C, \kappa^V$), at both the state- and county-level of geographic resolution. In addition, for the state-level model, it also influences the hospitalization rate h , ICU rate c and ventilator rate v .

Hospital Resource Availability. We posit that when an epidemic of like COVID-19 strikes a community with such a rapid progression, local hospital resources can quickly become overwhelmed [32]. We use the BigQuery public dataset that comes from the Center for Medicare and Medicaid Services, a federal agency within the United States Department of Health and Human Services (bigquery-public-data:cms_medicare.hospital_general_info). These static covariates are encoded into the diagnosis rate (γ), recovery rates ($\rho^{(I,d)}$, $\rho^{(I,u)}$, $\rho^{(H)}$, $\rho^{(C)}$, $\rho^{(V)}$), re-infected rate (η) and death rate ($\kappa^{(I,d)}$, κ^H , κ^C , κ^V), at both the state- and county-level of geographic resolution.

Confirmed Cases and Deaths. Past confirmed case counts and deaths can have an effect on the current values of these quantities. We include these as temporal covariates. These have an effect on the average contact rates ($\beta^{(d)}$, $\beta^{(u)}$), the diagnosis rate (γ) and the hospitalization rate h .

B Comparisons to IHME model

In this section, we include the comparison of our model with Institute for Health Metrics and Evaluation (IHME) [28] model, which has been used by major US government organizations. IHME is based on curve-fitting considering the nonlinear mixing effects with intervention assumptions. Since the provided prediction dates are different for IHME model, we run separate comparisons for it in 12-day ahead forecasting setting (still using our 14-day forecasts). As Table 6 shows, our model significantly outperforms IHME, consistently across all phases of the disease.

Table 6: τ -day ahead MAE for 12-day forecasting the number of deaths at state-level.

Pred. horizon τ (days)	Pred. date	Ours	IHME
12	05/05/2020	128.6	146.8
	05/19/2020	56.1	116.1
	06/09/2020	43.4	60.5
	06/23/2020	81.4	99.8
	08/25/2020	36.3	106.3
	09/22/2020	40.7	69.6

C Comparisons to Berkeley Yu model

In this section we include more comparisons of our model with the Berkeley Yu model [44] on more recent dates. As Table 7 shows, our model consistently outperforms Berkeley Yu model.

Table 7: τ -day average MAE for 7-day forecasting the number of deaths at county-level.

Pred. date	Ours	Berkeley-Yu
2020/06/02	0.8	1.82
2020/06/09	1.02	1.79
2020/06/16	0.9	1.75
2020/07/21	1.11	2.11
2020/07/28	1.33	2.68
2020/08/11	1.36	2.33
2020/08/18	1.35	2.27

D Prediction intervals of confirmed cases

E Impact of data quality

For fair comparison, we used the data available on the prediction date for model development (training and model selection), and we use the data from τ days later after the prediction date for evaluation. There are numerous data quality issues which are often corrected later. It is not unlikely to see that the number of confirmed or death cases for a particular day are significantly increased or decreased few weeks (and sometimes few months) later. Unfortunately, such data quality issues often have unpredictable patterns (due to human entry errors, reporting changes, or infrastructure issues) and can be treated as input ‘noise’. The accuracy of our model also suffers from them. To demonstrate the

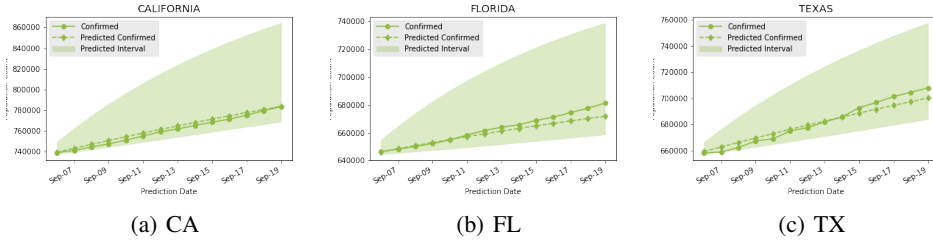


Figure 8: Prediction intervals of confirmed cases for 14-day forecasting. We use the 10-th and the 90-th quantile prediction as the the lower and the upper bound of prediction intervals, respectively.

impact of data quality issues, we perform experiments by training and evaluating our model with the most recent version of the data (from October), on different cases (note that we still have the same time-series split for training, validation and test). Table 8 shows the significant difference in results and the potential of our model with better quality data.

Table 8: τ -day average MAE for 14-day forecasting the number of deaths at state-level.

Pred. horizon τ (days)	Pred. date	Ours (data version of pred. date)	Ours (recent data version)
14	06/02/2020	32.8	29.6
	06/09/2020	28.8	23.2
	06/16/2020	31.4	20.9

F Rate variable definitions

Table 9: Variables and the covariates that affect them. (doc.: documented, undoc.: undocumented)

Variable	Description	Covariates
β	Average contacts of doc. infected ($\beta^{(d)}$) / undoc. infected ($\beta^{(u)}$)	Mobility, Interventions, Density
η	Re-infected rate	Census, Healthcare
α	Inverse latency period	-
γ	Diagnosis rate	Census, Test info
h	Hospitalization rate for infected	Census, Income, Healthcare
c	ICU rate for hospitalized	
v	Ventilator rate from ICU	
ρ	Recovery rate for doc. infected ($\rho^{(I,d)}$), undoc. infected ($\rho^{(I,u)}$), hospitalized ($\rho^{(H)}$), ICU ($\rho^{(U)}$), ventilator ($\rho^{(V)}$)	
κ	Death rate for doc. infected ($\kappa^{(I,d)}$), hospitalized ($\kappa^{(H)}$), ICU ($\kappa^{(C)}$), ventilator ($\kappa^{(V)}$)	

G Effective reproduction number

The effective reproduction number R_e is the expected number of new infections arising directly from one infected individual in a population where all individuals are susceptible to infection [34]. For example, the R_e for COVID-19 during the early stages of the pandemic in Wuhan, China has been estimated to be around 5.7 [51].

The Next-Generation Matrix [34] is a method to derive expressions for the R_e from a given compartment model. The method involves first finding the disease-free equilibrium (DFE) of the model. The infected sub-system of the compartment model at DFE is identified and its corresponding differential equations are isolated. Then the inflow and outflow terms from each compartment in the sub-system are partitioned between two categories—(i) new infection causing events and (ii) all other flows between compartments.

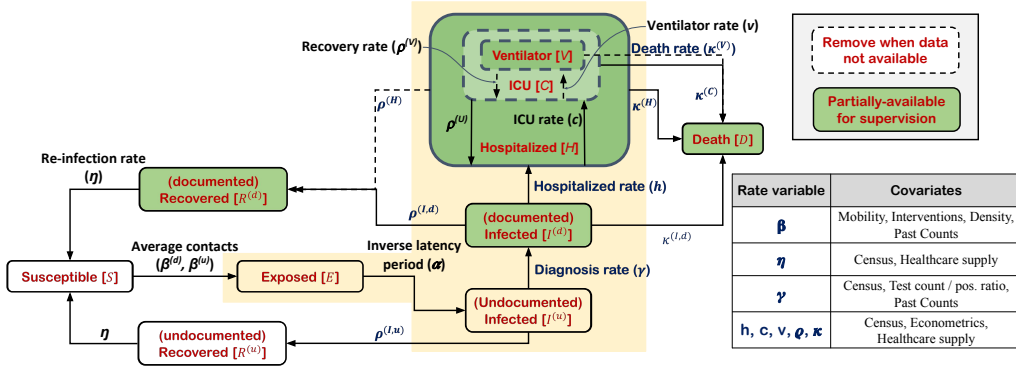


Figure 9: Our compartment model with the infection compartments highlighted, and the variables from Table 9 indicated next to each transition.

Two matrices—the new infections matrix \mathbf{F} and the transitions matrix \mathbf{V} —are constructed from the inflow and outflow terms.

The DFE for our model is $[S, E, I^{(d)}, I^{(u)}, R^{(d)}, R^{(u)}, H, C, V, D] = [N, 0, 0, 0, 0, 0, 0, 0, 0, 0]$. We begin by isolating the infection subsystem as shown in Figure 9. All the individuals in these compartments $\vec{X} \equiv [E, I^{(d)}, I^{(u)}, H, C, V]$ are at some stage of the infection. The individuals in $\vec{Y} \equiv [S, R^{(d)}, R^{(u)}, D]$ are not infected. From the system of difference equations in Section 3, the differential equations for the infection subsystem reduces to:

$$\begin{aligned}
 \dot{E} &= (\beta^{(d)} \cdot I^{(d)} + \beta^{(u)} \cdot I^{(u)}) \cdot S/N_i - \alpha \cdot E \\
 \dot{I}^{(d)} &= \gamma \cdot I^{(u)} - (\rho^{(I,d)} + \kappa^{(I,d)} + h) \cdot I^{(d)} \\
 \dot{I}^{(u)} &= \alpha \cdot E - (\rho^{(I,u)} + \gamma) \cdot I^{(u)} \\
 \dot{H} &= h \cdot I^{(d)} - \kappa^C \cdot (C - V) - \kappa^V \cdot V - (\kappa^{(H)} + \rho^{(H)}) \cdot (H - C) \\
 \dot{C} &= c \cdot (H - C) - (\kappa^{(C)} + \rho^{(C)} + v) \cdot (C - V) + \kappa^{(V)} \cdot V \\
 \dot{V} &= v \cdot (C - V) - (\kappa^{(V)} + \rho^{(V)}) \cdot V
 \end{aligned} \tag{5}$$

At the DFE, the subsystem is:

$$\begin{aligned}
 \dot{E} &= (\beta^{(d)} \cdot I^{(d)} + \beta^{(u)} \cdot I^{(u)}) - \alpha \cdot E \\
 \dot{I}^{(d)} &= \gamma \cdot I^{(u)} - (\rho^{(I,d)} + \kappa^{(I,d)} + h) \cdot I^{(d)} \\
 \dot{I}^{(u)} &= \alpha \cdot E - (\rho^{(I,u)} + \gamma) \cdot I^{(u)} \\
 \dot{H} &= h \cdot I^{(d)} - \kappa^C \cdot (C - V) - \kappa^V \cdot V - (\kappa^{(H)} + \rho^{(H)}) \cdot (H - C) \\
 \dot{C} &= c \cdot (H - C) - (\kappa^{(C)} + \rho^{(C)} + v) \cdot (C - V) + \kappa^{(V)} \cdot V \\
 \dot{V} &= v \cdot (C - V) - (\kappa^{(V)} + \rho^{(V)}) \cdot V
 \end{aligned} \tag{6}$$

Examining the right-hand side of the system of equations 5, we see that it is of the form:

$$\dot{\vec{X}} = \mathbf{M} \times \vec{X} \tag{7}$$

where $\mathbf{X} \equiv [E, I^{(d)}, I^{(u)}, H, C, V]$ and \mathbf{M} is given by:

$$\begin{bmatrix} -\alpha & \beta^{(d)} & \beta^{(u)} & 0 & 0 & 0 \\ 0 & -h - \kappa^{(I,d)} - \rho^{(I,d)} & \gamma & 0 & 0 & 0 \\ \alpha & 0 & -\gamma - \rho^{(I,u)} & 0 & 0 & 0 \\ 0 & h & 0 & -\kappa^{(H)} - \rho^{(H)} & -\kappa^{(C)} + \kappa^{(H)} + \rho^{(H)} & \kappa^{(C)} - \kappa^{(V)} \\ 0 & 0 & 0 & c & -c - v - \kappa^{(C)} - \rho^{(C)} & \kappa^{(C)} - \kappa^{(V)} + \rho^{(C)} + v \\ 0 & 0 & 0 & 0 & v & -\kappa^{(V)} - \rho^{(V)} - v \end{bmatrix} \quad (8)$$

Upon examination of Figure 9, we see that the only new-infection causing events are described by the rates $\beta^{(d)}$ and $\beta^{(u)}$. We define the new infections matrix \mathbf{F} as:

$$\begin{bmatrix} 0 & \beta^{(d)} & \beta^{(u)} & 0 & 0 & 0 \\ 0 & 0 & 0 & 0 & 0 & 0 \\ 0 & 0 & 0 & 0 & 0 & 0 \\ 0 & 0 & 0 & 0 & 0 & 0 \\ 0 & 0 & 0 & 0 & 0 & 0 \\ 0 & 0 & 0 & 0 & 0 & 0 \end{bmatrix} \quad (9)$$

We calculate the transitions matrix $\mathbf{V} = -(\mathbf{M} - \mathbf{F})$ to be:

$$\begin{bmatrix} \alpha & 0 & 0 & 0 & 0 & 0 \\ 0 & h + \kappa^{(I,d)} + \rho^{(I,d)} & -\gamma & 0 & 0 & 0 \\ -\alpha & 0 & \gamma + \rho^{(I,u)} & 0 & 0 & 0 \\ 0 & -h & 0 & \kappa^{(H)} + \rho^{(H)} & \kappa^{(C)} - \kappa^{(H)} - \rho^{(H)} & -\kappa^{(C)} + \kappa^{(V)} \\ 0 & 0 & 0 & -c & c + v + \kappa^{(C)} + \rho^{(C)} & -\kappa^{(C)} + \kappa^{(V)} - \rho^{(C)} - v \\ 0 & 0 & 0 & 0 & -v & \kappa^{(V)} + \rho^{(V)} + v \end{bmatrix} \quad (10)$$

From \mathbf{F} and \mathbf{V} we get the Next-Generation Matrix $\mathbf{K} = \mathbf{F} \times \mathbf{V}^{-1}$:

$$\begin{bmatrix} \frac{\beta^{(d)}\gamma}{(\gamma + \rho^{(I,u)})(h + \kappa^{(I,d)} + \rho^{(I,d)})} + \frac{\beta^{(u)}}{\gamma + \rho^{(I,u)}} & \frac{\beta^{(d)}}{h + \kappa^{(I,d)} + \rho^{(I,d)}} & \frac{\beta^{(d)}\gamma}{(\gamma + \rho^{(I,u)})(h + \kappa^{(I,d)} + \rho^{(I,d)})} + \frac{\beta^{(u)}}{\gamma + \rho^{(I,u)}} & 0 & 0 & 0 \\ 0 & 0 & 0 & 0 & 0 & 0 \\ 0 & 0 & 0 & 0 & 0 & 0 \\ 0 & 0 & 0 & 0 & 0 & 0 \\ 0 & 0 & 0 & 0 & 0 & 0 \end{bmatrix} \quad (11)$$

Calculating the eigenvalues of \mathbf{K} gives us 5 eigenvalues that are 0, and one non-zero eigenvalue, which is the spectral radius of \mathbf{K} . This is the effective reproduction number R_e :

$$R_0 = \frac{\beta^{(d)}\gamma + \beta^{(u)}(h + \kappa^{(I,d)} + \rho^{(I,d)})}{(\gamma + \rho^{(I,u)})(h + \kappa^{(I,d)} + \rho^{(I,d)})}. \quad (12)$$

H Training details

The start date of training is set to 1/21/2020. We assume that the compartmental equation regime start when the number of confirmed cases exceed 10 (before it, to avoid noise, we simple assign the initial values). We initialize the values as follows, where $\psi_{()} \sim U[0, 1]$ denote random variables with uniform distribution: $\hat{E}_i[0] = \max(100\psi_{E_{i,1}}, 10\psi_{E_{i,2}}Q_i[0])$, $\hat{I}_i^{(d)}[0] = Q_i[0]$, $\hat{I}_i^{(u)}[0] = \max(100\psi_{E_{i,1}}, 10\psi_{E_{i,2}}Q_i[0])$, $\hat{R}_i^{(d)}[0] = R[0]$, $\hat{R}_i^{(u)}[0] = 5\psi_{R_i}R[0]$, $\hat{H}_i[0] = \mathbb{I}\{H[0]\}H[0] + 0.5\psi_{H_i}(1 - \mathbb{I}\{H[0]\})Q[0]$, $\hat{C}_i[0] = \mathbb{I}\{C[0]\}C[0] + 0.2\psi_{C_i}(1 - \mathbb{I}\{C[0]\})Q[0]$ and $\hat{V}_i[0] = \mathbb{I}\{V[0]\}V[0] + (1 - 0.5\psi_{V_i}\mathbb{I}\{V[0]\})Q[0]$. In general, our model is not too sensitive to random initialization of the initial values, and we just define wide ranges to enable exploration.

I Hospitalization forecasts

Fig. 10 exemplifies fitted hospitalization predictions for 8 states. Our model can provide robust and accurate forecasts consistently (e.g. in increasing, decreasing or plateauing trends), despite the fluctuations in the past observed data.

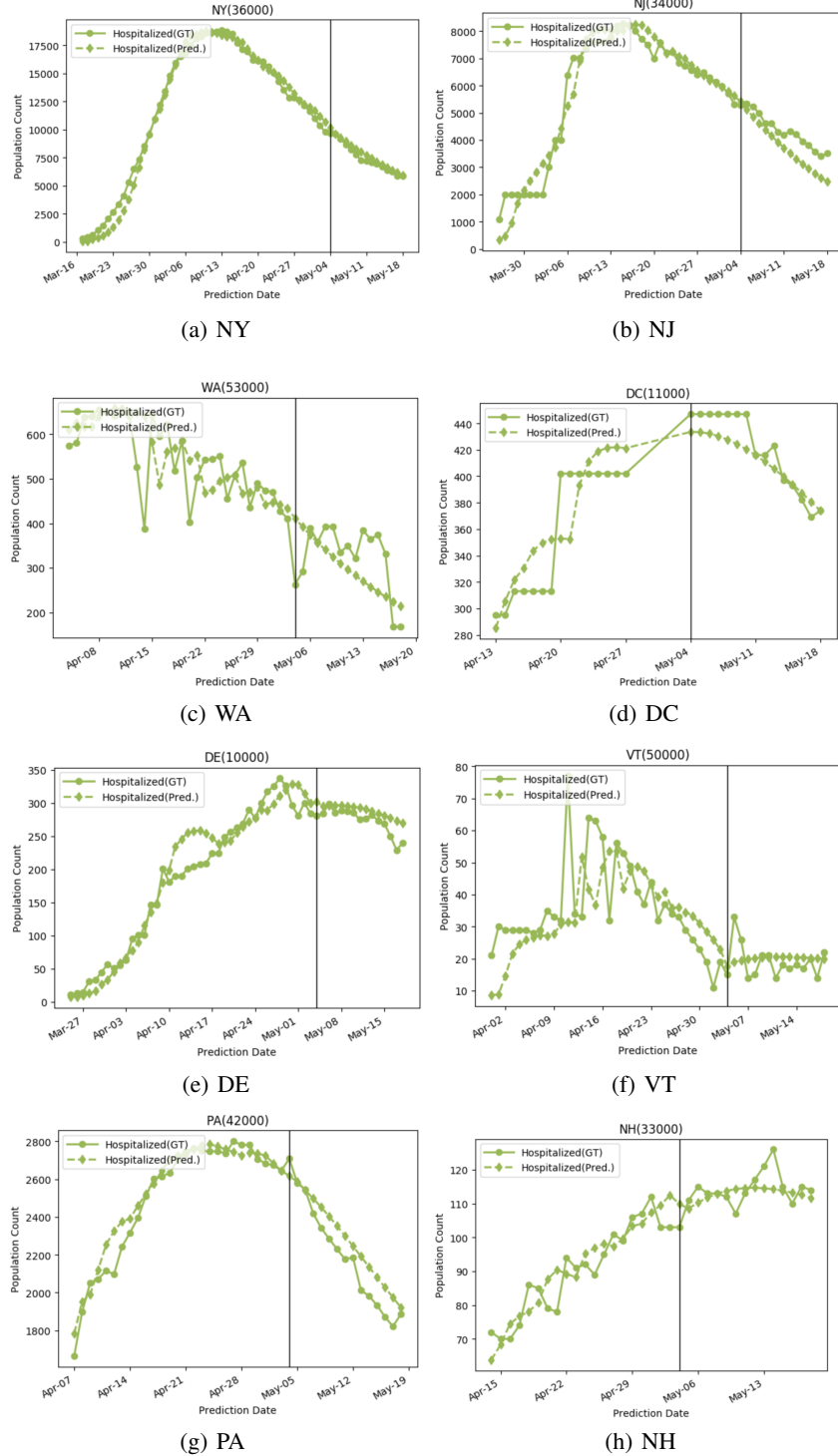


Figure 10: Fitted hospitalization compartments for 8 states. The vertical line shows the prediction date. Our model can provide robust and accurate forecasts, despite the highly-noisy observed data.

J State-level 14-day forecasts

We present the 14-day forecasts for all 50 US states.

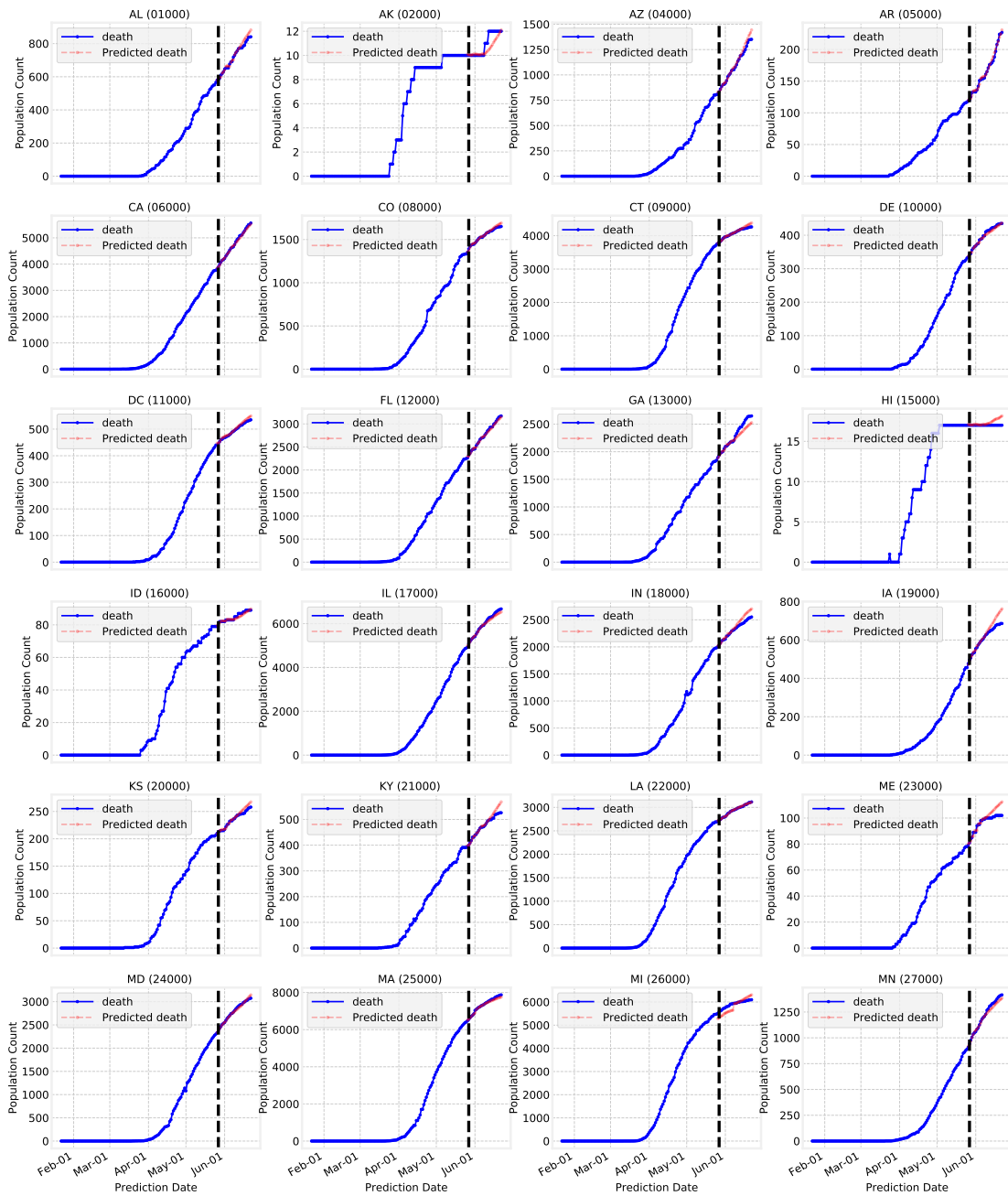


Figure 11: Model performance on US states—Alabama to Minnesota.

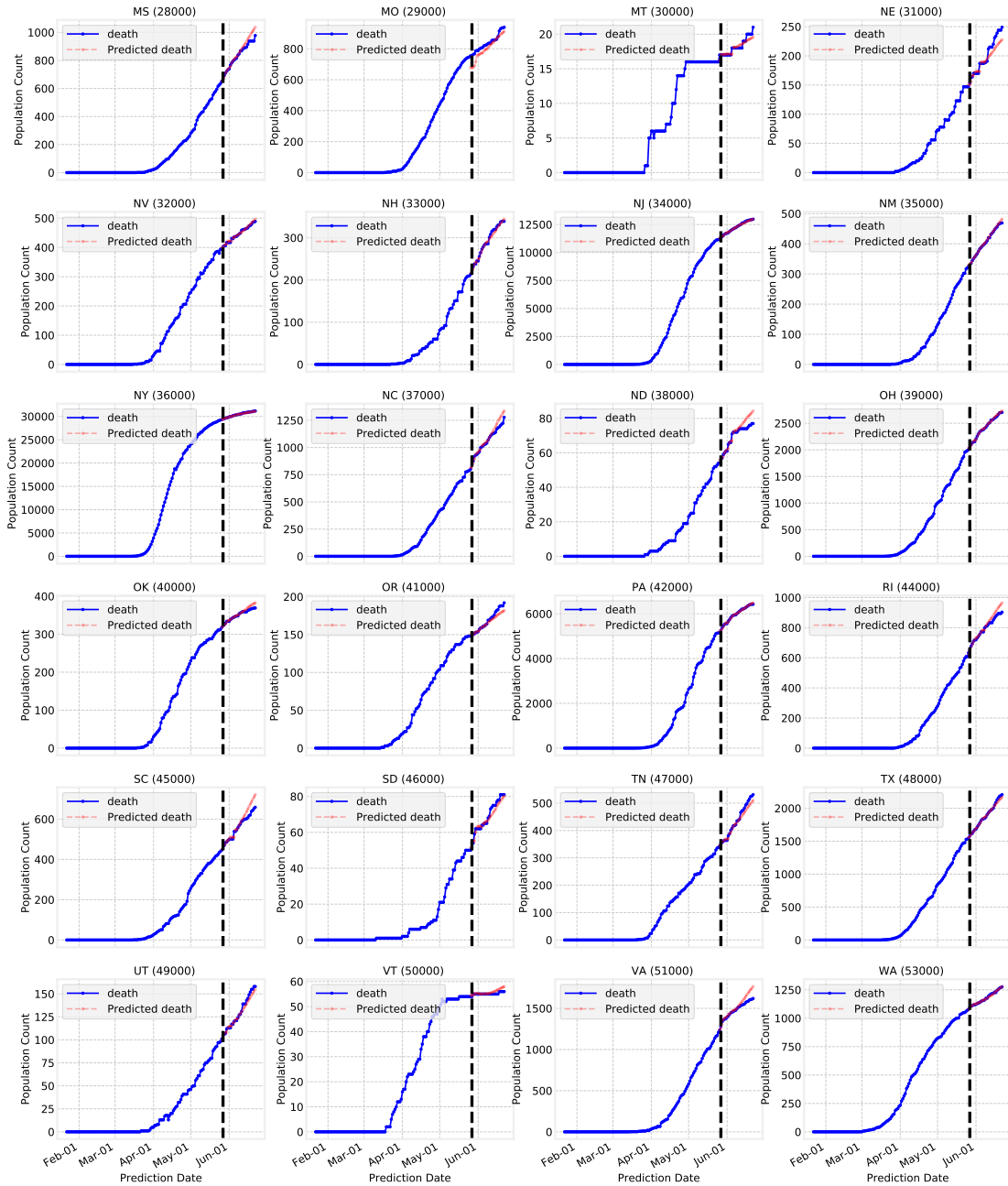


Figure 12: Model performance on US states–Missouri to Washington.

K County-level 14-day forecasts

We present the 14-day forecasts for selected US counties ordered by deaths from Covid-19.

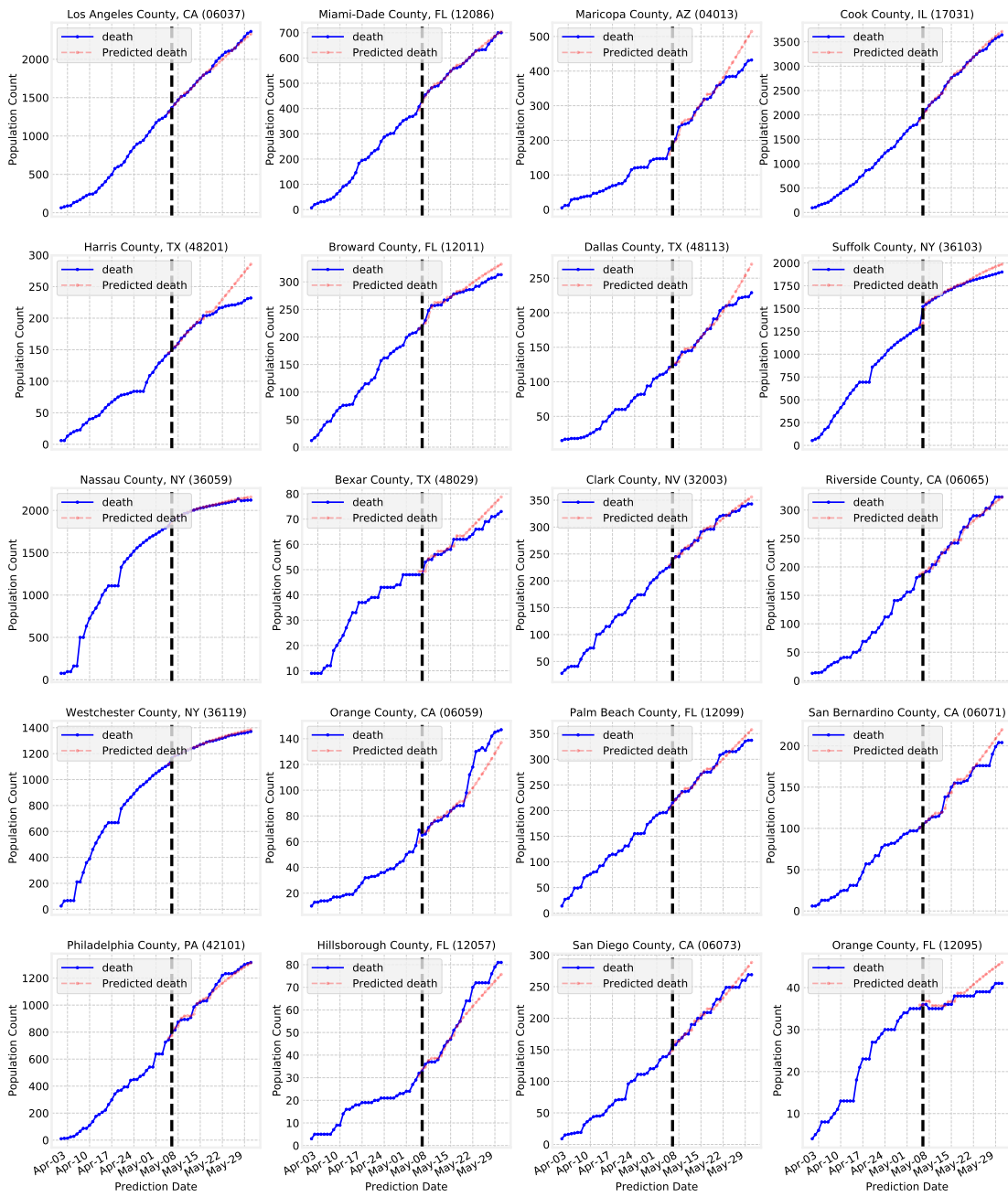


Figure 13: Model performance on selected US counties ordered by deaths.

L Potential limitations

In this section, we list the potential limitations and failure cases of our model, to guide those who may use the techniques to build forecasting systems that may effect public health decisions:

- **Ground-truth data issues:** We are using different case counts data to supervise model training. It has been noted that the ground truth case counts might not be completely accurate for various reasons, such as the practices to obtain case counts varying across locations [52, 53]. We have weighted optimization to balance supervision from different signals, e.g. we have higher weight on the supervision from the death case count because it is known to be more accurate. Yet, the case counts data quality may also vary across locations and may affect our model’s performance.
- **Failure to capture very rapid trend changes:** When the case count curves suddenly becomes very flat or very sharp, our model can fail to capture such dynamics. Some of such trends occur due to modifications in reporting practices, and some due to other factors that are not captured by the covariates we use. We believe more optimal temporal encoding approaches and integration of additional time-varying covariates may further mitigate this.
- **Using equal weight for all locations:** Our goal is to define a nation-wide metric that represents all individuals. We do not apply hand-tuned weighting for different locations, although it would be trivial with our framework. When equal weights are considered, the locations with the high case counts dominate the learning, which is often desired, but if any application requires a different emphasis mechanism, such as more accuracy for locations specifically with higher average age etc., the coefficient of the constituent locations’ loss terms can be re-weighted.
- **Having symmetry in loss:** Under- vs. over-prediction have different implications on public policy, socioeconomic dynamics and public health. Our framework allows penalizing them in an asymmetric way, and we have tried different weights but we could not obtain consistent improvements when the overall accuracy is considered. Instead of overall accuracy, if an application needs to focus on under- or over-prediction specifically, the model could be retrained for improved performance.
- **Performance differences among sub-groups:** As COVID-19 is affecting certain sub-groups more than others, the case counts are not uniformly distributed among the entire population. As absolute errors tend to be higher for greater case counts, there could be performance differences among different sub-groups. We do not observe our model to exacerbate the inherit case count differences (e.g. for racial and ethnic subgroups).
- **Overfitting to the past:** Especially in very early phases of the disease, our model may suffer from overfitting in some cases, as the past observations may not have sufficient information content for all the dynamics of the future. We have various mitigation mechanisms to prevent overfitting, but it is impossible to completely get rid of it. We overall observe improved performance relative to the benchmarks with more training data.
- **Prediction intervals and uncertainty:** Our approach to obtain prediction intervals is not based on Bayesian approaches [54, 55] per se (we do not estimate the posteriors of the parameters). We adapt quantile regression to obtain prediction intervals, and we cannot decouple the aleatoric (statistical) vs. epistemic (systematic) uncertainty inherent in the data and the model, while training. An ideal forecasting model should be able to decouple those and while providing accurate (point) forecasts, it should be able to tell the range of scenarios accurately (in a well-calibrated way). We leave such Bayesian approaches to improve our base ideas to future work.